

Characterization of Rh–Cr Mixed-Oxide Nanoparticles Dispersed on $(\text{Ga}_{1-x}\text{Zn}_x)(\text{N}_{1-x}\text{O}_x)$ as a Cocatalyst for Visible-Light-Driven Overall Water Splitting

Kazuhiko Maeda,[†] Kentaro Teramura,[†] Daling Lu,[‡] Tsuyoshi Takata,[†] Nobuo Saito,[§] Yasunobu Inoue,[§] and Kazunari Domen^{*,†,‡}

Department of Chemical System Engineering, The University of Tokyo, 7-3-1 Hongo, Bunkyo-ku, Tokyo 113-8656, Japan, Solution Oriented Research for Science and Technology (SORST) programs of the Japan Science and Technology Agency (JST), 4-1-8 Honcho, Kawaguchi-shi, Saitama 332-0012, Japan, and Department of Chemistry, Nagaoka University of Technology, Nagaoka 940-2188, Japan

Received: March 23, 2006; In Final Form: May 24, 2006

The structure of Rh–Cr mixed-oxide ($\text{Rh}_{2-y}\text{Cr}_y\text{O}_3$) nanoparticles dispersed on $(\text{Ga}_{1-x}\text{Zn}_x)(\text{N}_{1-x}\text{O}_x)$ is characterized by electron microscopy and X-ray spectroscopy. The $\text{Rh}_{2-y}\text{Cr}_y\text{O}_3$ nanoparticle is an efficient cocatalyst for photocatalytic overall water splitting on the $(\text{Ga}_{1-x}\text{Zn}_x)(\text{N}_{1-x}\text{O}_x)$ solid solution and is loaded onto the catalyst by impregnation from an aqueous solution containing $\text{Na}_3\text{RhCl}_6 \cdot 2\text{H}_2\text{O}$ and $\text{Cr}(\text{NO}_3)_3 \cdot 9\text{H}_2\text{O}$ followed by calcination in air. Impregnation of the $(\text{Ga}_{1-x}\text{Zn}_x)(\text{N}_{1-x}\text{O}_x)$ with 1 wt % Rh and 1.5 wt % Cr followed by calcination at 623 K for 1 h provides the highest photocatalytic activity. Structural analyses reveal that the activity of this photocatalyst is strongly dependent on the generation of trivalent Rh–Cr mixed-oxide nanoparticles with optimal composition and distribution.

1. Introduction

Hydrogen production by overall water splitting under solar radiation using a heterogeneous photocatalyst has attracted substantial interest in recent years as a potentially useful means of solar energy conversion. Among the various visible-light-driven photocatalysts reported to be active for H_2 or O_2 evolution from aqueous solutions containing a suitable sacrificial electron donor or acceptor,^{1–17} only the solid solution of GaN and ZnO with a wurtzite crystal structure¹⁸ shows reasonable photocatalytic activity for overall water splitting under visible light irradiation when modified with appropriate cocatalysts, such as RuO_2 ^{7–9} and Rh–Cr mixed-oxide nanoparticles.¹⁰ In particular, the solid solution modified with Rh–Cr mixed-oxide nanoparticles as H_2 evolution cocatalysts exhibits high photocatalytic activity for overall water splitting under visible light irradiation, achieving the highest quantum efficiency (ca. 2.5% at 420–440 nm)¹⁰ among particulate photocatalysts reported to be suitable for the reaction.

It is well-known that the photocatalytic activity for overall water splitting is strongly dependent on the structure of the loaded cocatalyst.^{9,19} It is therefore important to investigate the structural characteristics of the cocatalyst to develop a highly active photocatalyst. However, in contrast to well-characterized cocatalysts, such as NiO_x ¹⁹ and RuO_2 ,⁹ structural characterization of the Rh–Cr mixed-oxide cocatalyst has yet to be conducted and the relationship between the structure of the catalyst and the photocatalytic activity remains unclear.

In this study, the structural characteristics of the Rh–Cr mixed-oxide cocatalyst on the $(\text{Ga}_{1-x}\text{Zn}_x)(\text{N}_{1-x}\text{O}_x)$ surface were

investigated by scanning electron microscopy (SEM), high-resolution transmission electron microscopy (HR-TEM), X-ray photoelectron spectroscopy (XPS), and X-ray absorption spectroscopy (XAFS) in an attempt to clarify the relationship between the structure of the catalyst and the photocatalytic activity for overall water splitting under visible light irradiation.

2. Experimental Section

2.1. Materials and Reagents. The $(\text{Ga}_{1-x}\text{Zn}_x)(\text{N}_{1-x}\text{O}_x)$ solid solution was prepared according to the method present in previous papers.^{7,8} The production of $(\text{Ga}_{1-x}\text{Zn}_x)(\text{N}_{1-x}\text{O}_x)$ with $x = 0.12$ was confirmed by powder X-ray diffraction (XRD) and energy-dispersive X-ray (EDX) analysis.

$\text{Na}_3\text{RhCl}_6 \cdot 2\text{H}_2\text{O}$ (Kanto Chemicals, 97% as Rh) and $\text{Cr}(\text{NO}_3)_3 \cdot 9\text{H}_2\text{O}$ (Wako Pure Chemicals, 99.9%) were used as precursors for loading of the Rh–Cr mixed-oxide cocatalyst. For the measurement of XAFS and XPS spectra, Rh_2O_3 (Kanto Chemicals, 99.9%), Cr_2O_3 (Kanto Chemicals, 98.5%), and CrO_3 (Kanto Chemicals, 98.0%) were used as references. A solid solution of Rh_2O_3 and Cr_2O_3 ($\text{Rh}_{0.5}\text{Cr}_{1.5}\text{O}_3$) was prepared as a reference by the polymerized complex method.^{20,21}

2.2. Modification of $(\text{Ga}_{1-x}\text{Zn}_x)(\text{N}_{1-x}\text{O}_x)$ with Rh–Cr Mixed-Oxide Nanoparticles. Rh–Cr mixed-oxide nanoparticles as a cocatalyst were loaded onto the as-prepared $(\text{Ga}_{1-x}\text{Zn}_x)(\text{N}_{1-x}\text{O}_x)$ catalyst according to the method described previously.¹⁰ Briefly, 0.3–0.4 g of $(\text{Ga}_{1-x}\text{Zn}_x)(\text{N}_{1-x}\text{O}_x)$ powder and 3–4 mL of distilled water containing an appropriate amount of $\text{Na}_3\text{RhCl}_6 \cdot 2\text{H}_2\text{O}$ and $\text{Cr}(\text{NO}_3)_3 \cdot 9\text{H}_2\text{O}$ were placed into an evaporating dish over a water bath. The suspension was stirred using a glass rod to complete evaporation. The resulting powder was collected and heated in air at 523–673 K for 1 h. One set of samples was not calcined. In this paper, the amount of loaded metals is represented as metallic content.

2.3. Characterization of Catalysts. The prepared samples were studied by powder XRD (Rigaku RINT-UltimaIII; $\text{Cu K}\alpha$), EDX spectroscopy (Horiba Emax-7000), SEM (Hitachi S-4700),

* To whom correspondence should be addressed. E-mail: domen@chemsys.t.u-tokyo.ac.jp. Tel: +81-3-5841-1148. Fax: +81-3-5841-8838.

[†] The University of Tokyo.

[‡] Solution Oriented Research for Science and Technology programs of the Japan Science and Technology Agency.

[§] Nagaoka University of Technology.

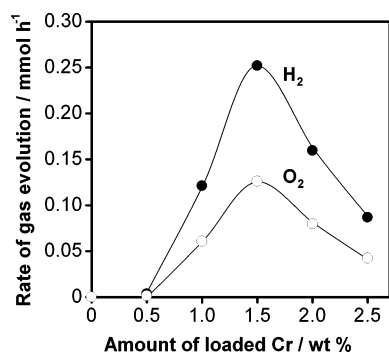


Figure 1. Dependence of the photocatalytic activity for overall water splitting under visible light irradiation ($\lambda > 400$ nm) on (Ga_{1-x}Zn_x)(N_{1-x}O_x) prepared with various loadings of Cr and a common amount of Rh (1 wt %) and calcination temperature of 623 K: catalyst, 0.3 g; distilled water, 370 mL; light source, high-pressure mercury lamp (450 W); inner-irradiation-type reaction vessel made of Pyrex with an aqueous NaNO₂ solution filter.

HR-TEM (JEOL JEM-2010F), XPS (Shimadzu ESCA-3200), and XAFS. XAFS measurements were carried out in the BL01B1 beamline of the SPring-8 synchrotron facility (Hyogo, Japan) using a ring energy of 8 GeV and stored current from 100 mA in top-up mode (Proposal No. 2004B0075-NXa-np) for the measurement of Rh–K edge spectra and in the BL12C beamline of the Photon Factory (High Energy Accelerator Research Organization, Tsukuba, Japan) using a ring energy of 2.5 GeV and stored current from 450 to 300 mA (Proposal No. 2004G317) for the measurement of Cr–K edge spectra. The X-ray absorption spectra were measured in transmission or fluorescence mode at room temperature with a Si(111) two-crystal monochromator. Data reduction was performed using the REX2000 program (Rigaku Corporation). The Fourier transforms of k^3 -weighted extended X-ray absorption fine structure (EXAFS) spectra were typically in the 3.0–12.0 Å region. The binding energies determined by XPS were corrected in reference to the Au4f_{7/2} peak (83.8 eV) for each sample.

2.4. Photocatalytic Reactions. Reactions were carried out in a Pyrex inner-irradiation-type reaction vessel connected to a glass closed gas circulation and evacuation system. The reactions were performed in distilled water containing 0.3 g of the cocatalyst-loaded sample. The reactant solution was evacuated several times to ensure complete air removal, followed by irradiation ($\lambda > 400$ nm) under a 450 W high-pressure mercury lamp via a Pyrex glass tube filled with NaNO₂ aqueous solution (2 M) to block ultraviolet (UV) light.^{7,8,10} It is considered that the 436 nm emission from the high-pressure mercury lamp is primarily responsible for driving the reaction.⁷ The evolved gases were analyzed by gas chromatography.

3. Results and Discussion

3.1. Effect of Cr Loading and Calcination Temperature on Photocatalytic Activity. As noted in the previous paper, (Ga_{1-x}Zn_x)(N_{1-x}O_x) modified with either Rh or Cr oxide exhibits little photocatalytic activity for overall water splitting.¹⁰ However, loading with both Rh and Cr results in stoichiometric H₂ and O₂ evolution. Figure 1 shows the dependence of the steady rate of H₂ and O₂ evolution on the amount of loaded Cr for samples calcined at 623 K after impregnation from an aqueous solution containing Na₃RhCl₆·2H₂O (1 wt % Rh) and Cr(NO₃)₃·9H₂O. H₂ and O₂ evolved stoichiometrically at Cr loadings of 0.5 wt % (H₂, 5.3 μmol·h⁻¹; O₂, 2.6 μmol·h⁻¹). The rates of H₂ and O₂ evolution increased markedly with Cr content to a maximum at 1.5 wt %, then decreased upon further loading.

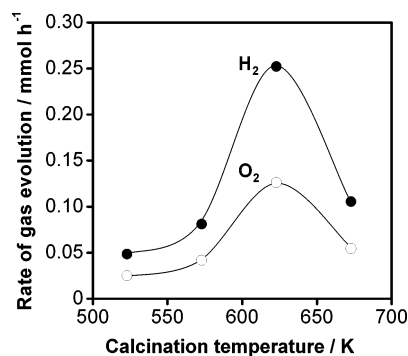


Figure 2. Dependence of the photocatalytic activity for overall water splitting under visible light irradiation ($\lambda > 400$ nm) on 1 wt % of Rh and 1.5 wt % of Cr-loaded (Ga_{1-x}Zn_x)(N_{1-x}O_x) after calcination at various temperatures: catalyst, 0.3 g; distilled water, 370 mL; light source, high-pressure mercury lamp (450 W); inner-irradiation-type reaction vessel made of Pyrex with an aqueous NaNO₂ solution filter.

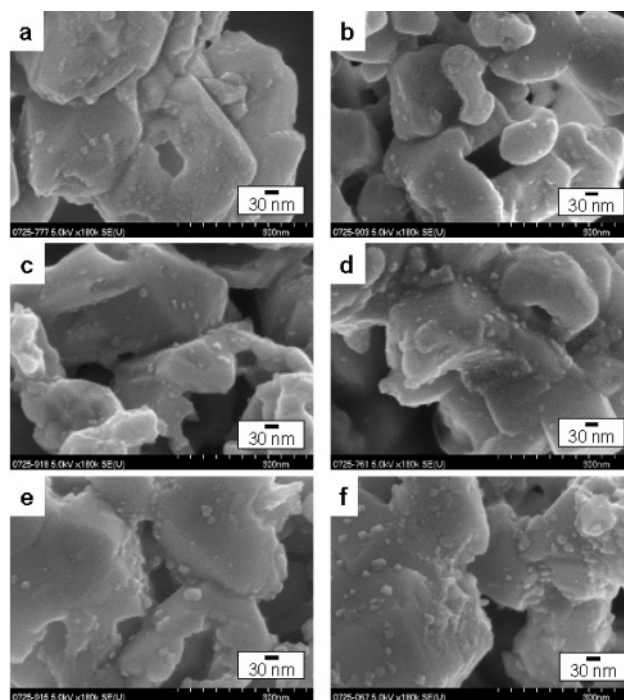


Figure 3. SEM images of (Ga_{1-x}Zn_x)(N_{1-x}O_x) loaded with 1 wt % Rh and (a) 0, (b) 0.5, (c) 1, (d) 1.5, (e) 2, and (f) 2.5 wt % Cr followed by calcination at 623 K.

Figure 2 shows the dependence of the rate of H₂ and O₂ evolution on calcination temperature after impregnation with 1 wt % Rh and 1.5 wt % Cr. The catalyst prepared without calcination did not produce H₂ or O₂. The rates of H₂ and O₂ evolution increased significantly with increasing calcination temperature to a maximum at 623 K, beyond which the activity of the samples began to decrease.

3.2. SEM and TEM Observations. The morphology of the prepared samples was observed by SEM. Figure 3 shows SEM images of various catalyst compositions of Cr with a common amount of loaded Rh (1 wt %) calcined at the optimal temperature of 623 K. All prepared samples exhibited a good distribution of fine primary particles with an average diameter of 10–30 nm deposited on larger (Ga_{1-x}Zn_x)(N_{1-x}O_x) particles, and the particle size increased with increasing Cr content.

Figure 4 shows SEM images of the samples with 1 wt % Rh and 1.5 wt % Cr after calcination at various temperatures. In the sample prepared without calcination, no particles were observed on the (Ga_{1-x}Zn_x)(N_{1-x}O_x) surface. However, above

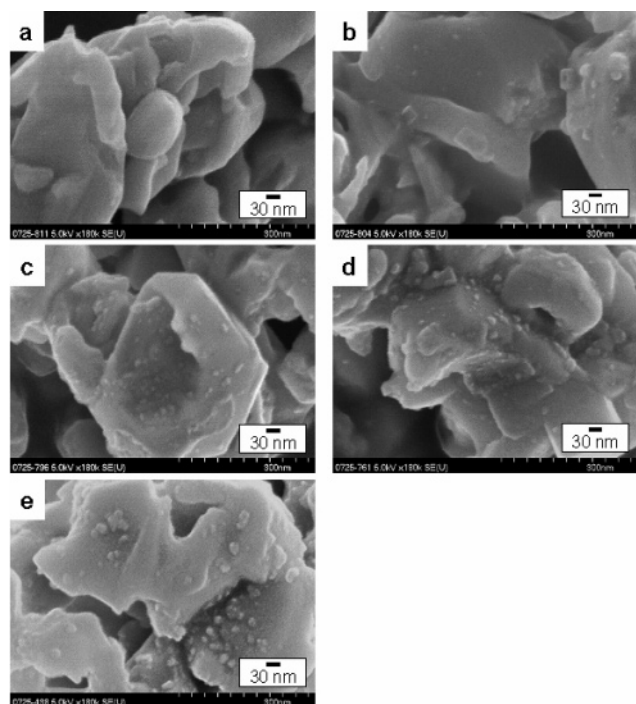


Figure 4. SEM images of $(\text{Ga}_{1-x}\text{Zn}_x)(\text{Ni}_{1-x}\text{O}_x)$ loaded with 1 wt % Rh and 1.5 wt % Cr (a) without calcination and (b–e) after calcination at (b) 523, (c) 573, (d) 623, and (e) 673 K.

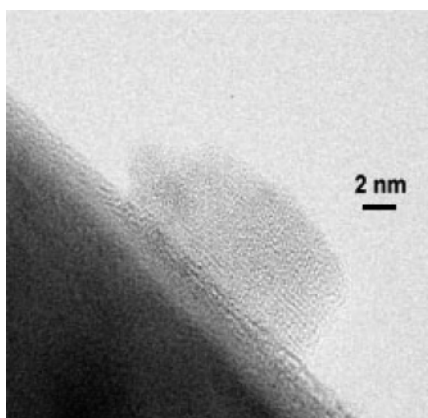


Figure 5. HR-TEM image of $(\text{Ga}_{1-x}\text{Zn}_x)(\text{Ni}_{1-x}\text{O}_x)$ loaded with 1 wt % Rh and 1.5 wt % Cr followed by calcination at 623 K.

523 K, fine particles of 5–20 nm in size began to appear, growing with increasing calcination temperature. At the highest calcination temperature of 673 K, nanoparticles of larger than 30 nm formed, with some aggregation. A HR-TEM image of the sample with 1 wt % Rh and 1.5 wt % Cr compositions after calcination at 623 K is shown in Figure 5. The lattice fringes in the HR-TEM image indicate that the loaded nanoparticles are crystalline. The results of combined TEM-EDS analyses for this sample are listed in Table 1. Although the ratio of Rh to Cr in nanoparticles varied somewhat, it is clear that these nanoparticles contained both Rh and Cr, indicating that the loaded nanoparticles were mixed-oxides of Rh and Cr. It has been reported by Wold et al. that Rh_2O_3 and Cr_2O_3 form a solid solution ($\text{Rh}_{2-y}\text{Cr}_y\text{O}_3$) with a corundum structure.²²

3.3. XPS Measurements. The valence state of Rh and Cr in the nanoparticles was investigated by XPS measurements. Figure 6 shows the XPS spectra for Rh3d and Cr2p in the sample with the 1 wt % Rh and 1.5 wt % Cr after calcination at 623 K. The data for Rh_2O_3 , $\text{Rh}_{0.5}\text{Cr}_{1.5}\text{O}_3$, and Cr_2O_3 are shown for reference. The Rh3d_{5/2} peak for Rh_2O_3 appears at 308.3 eV, in good

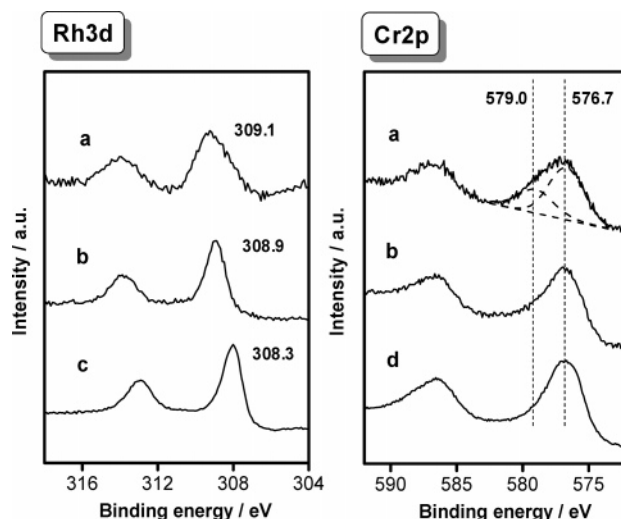


Figure 6. XPS spectra for Rh3d and Cr2p of (a) $(\text{Ga}_{1-x}\text{Zn}_x)(\text{Ni}_{1-x}\text{O}_x)$ loaded with 1 wt % Rh and 1.5 wt % Cr and calcined at 623 K, (b) $\text{Rh}_{0.5}\text{Cr}_{1.5}\text{O}_3$, (c) Rh_2O_3 , and (d) Cr_2O_3 .

TABLE 1: Result of TEM-EDS Analyses for 1 wt % Rh and 1.5 wt % Cr-Loaded $(\text{Ga}_{1-x}\text{Zn}_x)(\text{Ni}_{1-x}\text{O}_x)$ Calcined at 623 K

number of samples	elements/mol %		
	Rh	Cr	Rh/Cr ratio
1	0.33	2.24	0.15
2	0.71	3.13	0.23
3	0.92	8.45	0.11
4	1.83	3.19	0.57
5	0.58	1.4	0.41
in starting material			0.33

agreement with the reported values (308.4 eV,²³ 308.3 eV²⁴). However, the Rh3d_{5/2} peak for the sample appears at higher binding energy (309.1 eV) than for Rh_2O_3 (308.3 eV) and is close to the value for $\text{Rh}_{0.5}\text{Cr}_{1.5}\text{O}_3$ (308.9 eV), indicating that Rh and Cr interact within individual nanoparticles. This is supported by the results of EDS measurements. The reasons for which the shape of the Rh3d peak is relatively wide and slightly asymmetric would be the low loading amount of Rh (1 wt %) and the deviation of compositions in each nanoparticle (Table 1), respectively. The Cr2p_{3/2} peak for the sample is very close to that of the Cr_2O_3 reference (576.7 eV), although a small peak assignable to Cr^{6+} appears at ca. 579.0 eV.¹²

3.4. XAFS Measurements. Figure 7 shows the Rh–K and Cr–K edge X-ray absorption near-edge structure (XANES) spectra for a range of Cr compositions in samples with 1 wt % Rh after calcination at 623 K. Some reference data are shown for comparison. The Rh–K edge spectrum for the sample without Cr is similar to that for $\text{Na}_3\text{RhCl}_6 \cdot 2\text{H}_2\text{O}$ (spectrum a). However, with increasing Cr content, the Rh–K edge spectra become more similar to those for the Rh_2O_3 and $\text{Rh}_{0.5}\text{Cr}_{1.5}\text{O}_3$ references, indicating that the addition of Cr facilitates the decomposition of the precursor and the conversion to trivalent Rh–Cr mixed-oxide. The Rh–K edge spectra for these samples obviously differ from that for Rh foil. The Cr–K edge spectra, however, are all identical. Although a small preedge peak assigned to hexavalent Cr is observed for all prepared samples, the Cr–K edge spectra clearly differ from those for Cr foil and CrO_3 , and the spectral region around the absorption edge and ca. 6020 eV in the samples resembles those in the Cr_2O_3 and $\text{Rh}_{0.5}\text{Cr}_{1.5}\text{O}_3$ references.

Figure 8 shows the Fourier transforms of the k^3 -weighted Rh–K and Cr–K edge EXAFS spectra for the same samples.

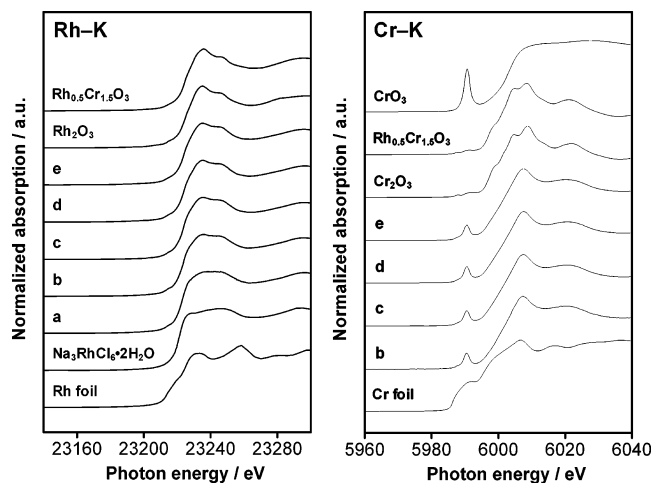


Figure 7. Rh–K and Cr–K edge XANES spectra for $(\text{Ga}_{1-x}\text{Zn}_x)(\text{Ni}_{1-x}\text{O}_x)$ loaded with 1 wt % Rh and (a) 0, (b) 0.5, (c) 1, (d) 1.5, and (e) 2 wt % Cr followed by calcination at 623 K.

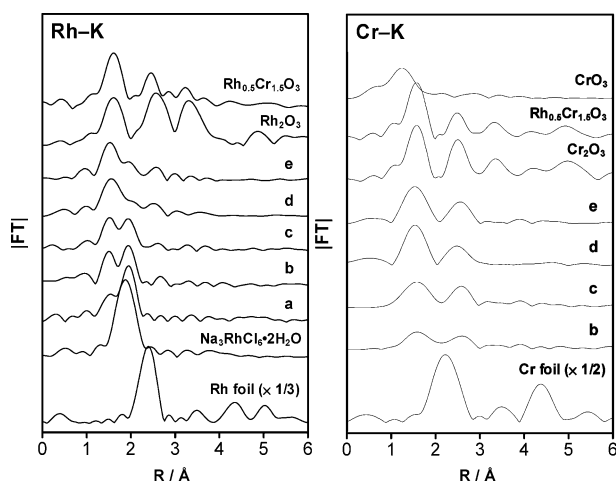


Figure 8. Fourier transforms of k^3 -weighted Rh–K and Cr–K edge EXAFS spectra for $(\text{Ga}_{1-x}\text{Zn}_x)(\text{Ni}_{1-x}\text{O}_x)$ loaded with 1 wt % Rh and (a) 0, (b) 0.5, (c) 1, (d) 1.5, and (e) 2 wt % Cr followed by calcination at 623 K.

In the Rh–K edge spectra, the sample without Cr exhibits a characteristic peak assignable to the Rh–Cl shell at ca. 1.9 Å (spectrum a). However, the peak intensity of the Rh–Cl shell decreases with increasing Cr content. The Cr–K edge spectrum for the 0.5 wt % Cr sample (spectrum b) displays relatively weak peaks assigned to the Cr–O (1.5 Å) and Cr–(O)–Cr or Rh (2.5 Å) shells. This suggests a small particle size, which is supported by the SEM observations (Figure 3b). The intensity of the peaks increased markedly with increasing Cr content, indicating that the size of the nanoparticles increased with increased Cr loading.

Figure 9 shows the Rh–K and Cr–K edge XANES spectra for samples with 1 wt % Rh and 1.5 wt % Cr after calcination at various temperatures. The data for some reference samples are shown for comparison. The Rh–K edge spectrum for the impregnated sample clearly differs from that of either Rh_2O_3 or $\text{Rh}_{0.5}\text{Cr}_{1.5}\text{O}_3$ (spectrum a) but is very similar to that of $\text{Na}_3\text{RhCl}_6 \cdot 2\text{H}_2\text{O}$. The spectra exhibit a change at 523 K and become similar to the spectra for the Rh_2O_3 and $\text{Rh}_{0.5}\text{Cr}_{1.5}\text{O}_3$ references above 623 K, indicating that the impregnated Rh species on the $(\text{Ga}_{1-x}\text{Zn}_x)(\text{Ni}_{1-x}\text{O}_x)$ surface decomposes and converts to trivalent Rh–Cr mixed-oxide at elevated calcination temperature. The Cr–K edge spectrum for the impregnated sample is identical to that for the $\text{Cr}(\text{NO}_3)_3 \cdot 9\text{H}_2\text{O}$ precursor (spectrum a).

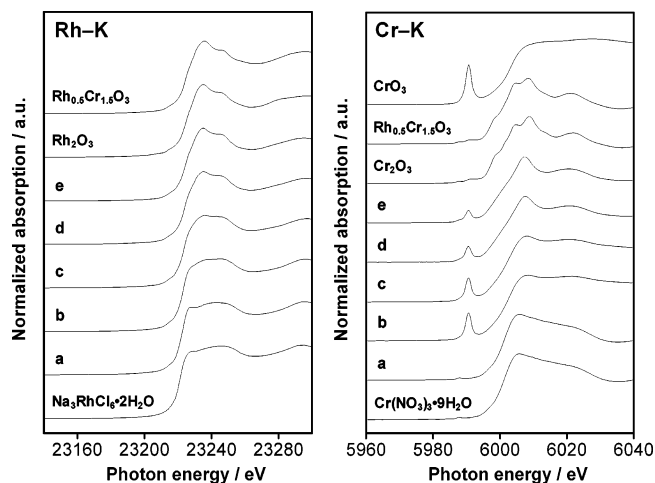


Figure 9. Rh–K and Cr–K edge XANES spectra for $(\text{Ga}_{1-x}\text{Zn}_x)(\text{Ni}_{1-x}\text{O}_x)$ loaded with 1 wt % Rh and 1.5 wt % Cr (a) without calcination and (b–e) followed by calcination at (b) 523, (c) 573, (d) 623, and (e) 673 K.

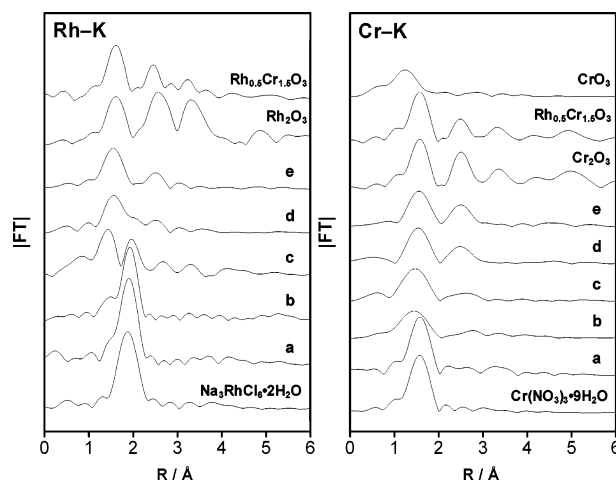


Figure 10. Fourier transforms of k^3 -weighted Rh–K and Cr–K edge EXAFS spectra for $(\text{Ga}_{1-x}\text{Zn}_x)(\text{Ni}_{1-x}\text{O}_x)$ loaded with 1 wt % Rh and 1.5 wt % Cr (a) without calcination and (b–e) followed by calcination at (b) 523, (c) 573, (d) 623, and (e) 673 K.

The shape of the spectrum changes remarkably with increasing calcination temperature. Calcination at 523 K results in the emergence of a preedge peak assigned to Cr^{6+} (spectrum b), but this preedge peak becomes weaker with increasing calcination temperature, and the spectrum becomes similar to the spectra for Cr_2O_3 and $\text{Rh}_{0.5}\text{Cr}_{1.5}\text{O}_3$. The weakening of the preedge peak assigned to Cr^{6+} is reasonable, since Cr(VI) oxide melts at 470 K and decomposes at 573 K.²⁵

Figure 10 shows the Fourier transforms of the k^3 -weighted Rh–K and Cr–K edge EXAFS spectra for the same samples. The peak assigned to the Rh–Cl shell appears at ca. 1.9 Å in both the noncalcined sample (spectrum a) and samples calcined below 573 K (spectra b and c), indicating that the structure of $\text{Na}_3\text{RhCl}_6 \cdot 2\text{H}_2\text{O}$ is partially preserved upon calcination at temperatures below 573 K. However, the characteristic peak weakens with increasing calcination temperature and is undetectable at 673 K (spectrum e), in good agreement with the change in the Rh–K edge XANES spectra (Figure 9). The peak at ca. 2.5 Å, attributable to Rh–(O)–Rh or Cr, also becomes stronger with increasing calcination temperature. In the Cr–K edge EXAFS spectra, although comparison with the first Cr–O shell peak at ca. 1.5 Å is difficult due to overlap by the peak derived from $\text{Cr}(\text{NO}_3)_3 \cdot 9\text{H}_2\text{O}$, the peak assigned to Cr–(O)–

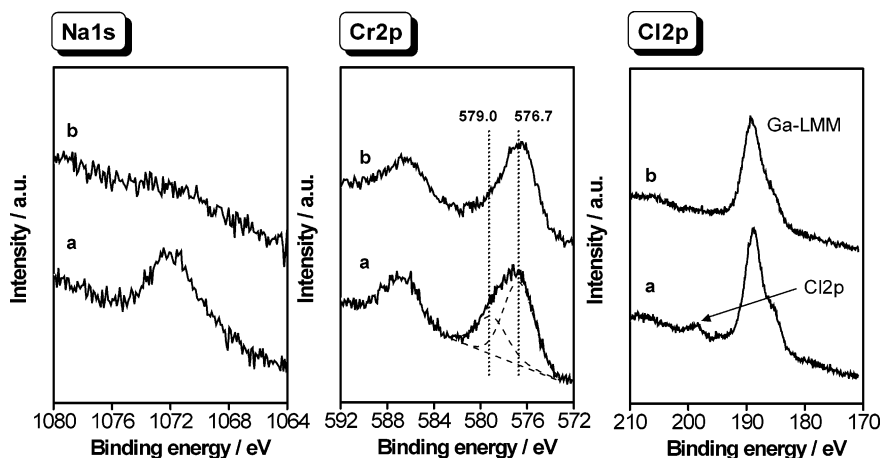


Figure 11. XPS spectra for Na1s, Cr2p, and Cl2p of $(\text{Ga}_{1-x}\text{Zn}_x)(\text{N}_{1-x}\text{O}_x)$ loaded with 1 wt % Rh and 1.5 wt % Cr followed by calcination at 623 K (a) before and (b) after water treatment.

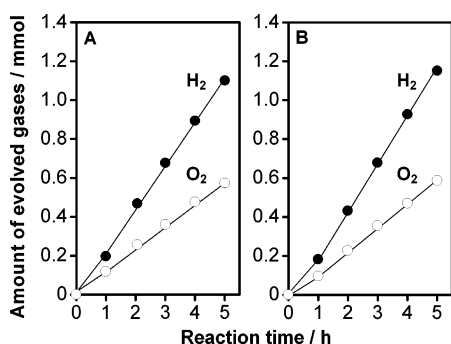


Figure 12. Time courses of overall water splitting under visible light irradiation ($\lambda > 400$ nm) on $(\text{Ga}_{1-x}\text{Zn}_x)(\text{N}_{1-x}\text{O}_x)$ loaded with 1 wt % Rh and 1.5 wt % Cr followed by calcination at 623 K (A) before and (B) after water treatment: catalyst, 0.3 g; distilled water, 370 mL; light source, high-pressure mercury lamp (450 W); inner-irradiation-type reaction vessel made of Pyrex with an aqueous NaNO_2 solution filter.

Cr or Rh at ca. 2.5 \AA becomes markedly more intense with increasing calcination temperature.

On the basis of the above analyses, it can be concluded that increases in the Cr content and calcination temperature lead to the formation of trivalent Rh–Cr mixed-oxide from the corre-

sponding Rh and Cr precursors and an increase in its particle size as indicated by the SEM observations.

It is presumed that active species for photocatalytic overall water splitting on $(\text{Ga}_{1-x}\text{Zn}_x)(\text{N}_{1-x}\text{O}_x)$ are trivalent Rh and Cr mixed-oxide ($\text{Rh}_{2-y}\text{Cr}_y\text{O}_3$) nanoparticles. However, Cr^{6+} , Na^+ , and Cl^- were detected by XPS after cocatalyst impregnation, as shown in Figure 11. The influence of such remnants on the photocatalytic activity for overall water splitting was investigated by comparing the activity before and after water treatment for removal of the remnants. It was confirmed by XPS that the remnants were completely removed from the catalyst surface by water treatment (Figure 11). As shown in Figure 12, the samples before and after treatment both achieved the same rates of stoichiometric H_2 and O_2 evolution in the initial stage of the reaction, indicating that remnants such as Cr^{6+} , Na^+ , and Cl^- have a negligible impact on the photocatalytic activity for overall water splitting. As shown in Figures 7–10, XAFS measurements reveal that the sample without Cr contains Rh–Cl species, which may also obstruct the photocatalytic decomposition of water. A Rh_2O_3 -loaded $(\text{Ga}_{1-x}\text{Zn}_x)(\text{N}_{1-x}\text{O}_x)$ sample impregnated from an $\text{Rh}(\text{NO}_3)_3$ precursor was found to exhibit very little photocatalytic activity for this reaction, indicating that the contribution

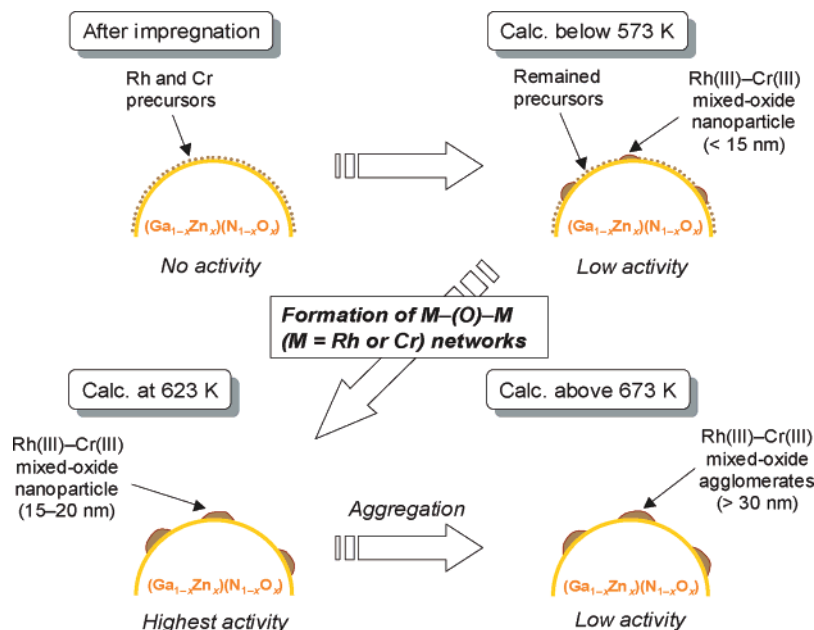


Figure 13. Schematic illustration of structural changes of Rh and Cr species on the $(\text{Ga}_{1-x}\text{Zn}_x)(\text{N}_{1-x}\text{O}_x)$ surface after various treatments.

of Cr in the Rh–Cr mixed-oxide nanoparticles is indispensable for enhancing the photocatalytic activity of this catalyst. Loading the $\text{Rh}_{2-y}\text{Cr}_y\text{O}_3$ cocatalyst from $\text{Rh}(\text{NO}_3)_3$ and $\text{Cr}(\text{NO}_3)_3 \cdot 9\text{H}_2\text{O}$ precursors achieved almost the same activity as the case in which $\text{Na}_3\text{RhCl}_6 \cdot 2\text{H}_2\text{O}$ and $\text{Cr}(\text{NO}_3)_3 \cdot 9\text{H}_2\text{O}$ precursors were used. It is thus concluded that the active species in this reaction are trivalent Rh and Cr mixed-oxide nanoparticles on the $(\text{Ga}_{1-x}\text{Zn}_x)(\text{N}_{1-x}\text{O}_x)$ surface.

3.5. Relationship between Catalyst Structure and Photocatalytic Activity. As shown in Figure 1, the photocatalytic activity was found to be strongly dependent on Cr. In the range between 0 and 1.5 wt % Cr content, in which the activity increased significantly, the structural characterization revealed that the cocatalyst particles became larger (Figure 3) and the loaded Rh species changed from the precursor form to the trivalent Rh–Cr mixed-oxide form (Figure 7). Furthermore, the first Cr–O and second Cr–(O)–Cr or Rh shell peak in the Cr–K edge EXAFS spectra became substantially stronger as the amount of Cr increased (Figure 8). Therefore, the increase in activity with increasing Cr is considered to be associated with the formation of trivalent Rh and Cr mixed-oxide nanoparticles. However, further loading more than 1.5 wt % Cr resulted in a decrease in activity, attributable to the aggregation of primary particles as observed in SEM images (Figure 3).

The calcination temperature was also found to be an important factor contributing to the enhancement of catalytic activity. The structural changes undergone by the catalyst in the various treatment steps are depicted schematically in Figure 13. XAFS measurements indicate that most of the loaded Rh and Cr species remain in the precursor form after impregnation (Figures 9 and 10). Calcination at 573 K results in the partial decomposition of the precursors and the formation of nanoparticles with an average diameter of less than 15 nm (Figure 4). However, upon calcination at higher temperatures, the nanoparticles transform into trivalent Rh–Cr mixed-oxide accompanied by particle growth, with some aggregation at 673 K. Accordingly, the increase in activity from 523 to 623 K is considered to be primarily due to the formation of active Rh–Cr mixed-oxide nanoparticles with trivalent electronic state, while the decrease in activity by calcination above 623 K can be attributable to the aggregation of nanoparticles. It can thus be concluded that the formation of trivalent Rh–Cr mixed-oxide nanoparticles with optimal composition and high dispersion on the catalyst surface is the most important factor in the enhancement of photocatalytic activity for overall water splitting over this catalyst. It is anticipated that the change in the electronic state of Rh by the incorporation of Cr also contributes to the enhancement of the photocatalytic activity, although this mechanism remains unclear and is under investigation.

4. Conclusion

The formation and structural characteristics of Rh and Cr species loaded on $(\text{Ga}_{1-x}\text{Zn}_x)(\text{N}_{1-x}\text{O}_x)$ as cocatalysts for photocatalytic overall water splitting were investigated. With increasing Cr content and calcination temperature, the loaded Rh and Cr species interact to form mixed-oxide nanoparticles with trivalent electronic state, resulting in an increase in activity for the water splitting reaction to maximum activity at 1 wt % Rh and 1.5 wt % Cr, with calcination at 623 K. Excess Cr

loading and higher calcination temperatures degraded activity from the maximum photocatalytic performance due to aggregation of nanoparticles. Nanoparticles of trivalent Rh and Cr mixed-oxide with optimal composition and distribution, as determined by the preparation conditions, were thus demonstrated to act as active species for photocatalytic overall water splitting.

Acknowledgment. This work was supported by the Solution Oriented Research for Science and Technology (SORST) program of the Japan Science and Technology (JST) Agency and the 21st Century Center of Excellence (COE) program of the Ministry of Education, Culture, Sports, Science and Technology of Japan.

References and Notes

- (1) Hitoki, G.; Takata, T.; Kondo, J. N.; Hara, M.; Kobayashi, H.; Domen, K. *Chem. Commun.* **2002**, 1698.
- (2) Hitoki, G.; Ishikawa, A.; Takata, T.; Kondo, J. N.; Hara, M.; Domen, K. *Chem. Lett.* **2002**, 31, 736.
- (3) Kasahara, A.; Nukumizu, K.; Hitoki, G.; Takata, T.; Kondo, J. N.; Hara, M.; Kobayashi, H.; Domen, K. *J. Phys. Chem. A* **2002**, 106, 6750.
- (4) Nukumizu, K.; Nunoshige, J.; Takata, T.; Kondo, J. N.; Hara, M.; Kobayashi, H.; Domen, K. *Chem. Lett.* **2003**, 32, 196.
- (5) Ishikawa, A.; Takata, T.; Kondo, J. N.; Hara, M.; Kobayashi, H.; Domen, K. *J. Am. Chem. Soc.* **2002**, 124, 13547.
- (6) Ishikawa, A.; Takata, T.; Matsumura, T.; Kondo, J. N.; Hara, M.; Kobayashi, H.; Domen, K. *J. Phys. Chem. B* **2004**, 108, 2637.
- (7) Maeda, K.; Takata, T.; Hara, M.; Saito, N.; Inoue, Y.; Kobayashi, H.; Domen, K. *J. Am. Chem. Soc.* **2005**, 127, 8286.
- (8) Maeda, K.; Teramura, K.; Takata, T.; Hara, M.; Saito, N.; Toda, K.; Inoue, Y.; Kobayashi, H.; Domen, K. *J. Phys. Chem. B* **2005**, 109, 20504.
- (9) Teramura, K.; Maeda, K.; Saito, T.; Takata, T.; Saito, N.; Inoue, Y.; Domen, K. *J. Phys. Chem. B* **2005**, 109, 21915.
- (10) Maeda, K.; Teramura, K.; Lu, D.; Takata, T.; Saito, N.; Inoue, Y.; Domen, K. *Nature* **2006**, 440, 295.
- (11) Kudo, A.; Mikami, I. *Chem. Lett.* **1998**, 27, 1027.
- (12) Kato, H.; Kudo, A. *J. Phys. Chem. B* **2002**, 106, 5029.
- (13) Kato, H.; Kobayashi, H.; Kudo, A. *J. Phys. Chem. B* **2002**, 106, 12441.
- (14) Konta, R.; Ishii, T.; Kato, H.; Kudo, A. *J. Phys. Chem. B* **2004**, 108, 8992.
- (15) Niishiro, R.; Kato, H.; Kudo, A. *Phys. Chem. Chem. Phys.* **2005**, 7, 2241.
- (16) Kim, H. G.; Hwang, D. W.; Lee, J. S. *J. Am. Chem. Soc.* **2004**, 126, 8912.
- (17) Kim, H. G.; Borse, P. H.; Choi, W.; Lee, J. S. *Angew. Chem., Int. Ed.* **2005**, 44, 4585.
- (18) Yashima, M.; Maeda, K.; Teramura, K.; Takata, T.; Domen, K. *Chem. Phys. Lett.* **2005**, 416, 225.
- (19) Domen, K.; Kudo, A.; Onishi, T.; Kosugi, N.; Kuroda, H. *J. Phys. Chem.* **1986**, 90, 292.
- (20) Kakihana, M.; Milanova, M. M.; Arima, M.; Okubo, T.; Yashima, M.; Yoshimura, M. *J. Am. Ceram. Soc.* **1996**, 79, 1673.
- (21) First, 0.9 g of $\text{Rh}(\text{NO}_3)_3$ and 3.74 g of $\text{Cr}(\text{NO}_3)_3 \cdot 9\text{H}_2\text{O}$ were dissolved in 100 mL of methanol (Kanto Chemical, 99.8%). After complete dissolution of the nitrates, 42 g of ethylene glycol (EG) (Kanto Chemicals, 99.5%) and 30 g of anhydrous citric acid (CA) (Wako Pure Chemicals, 98.0%) were added to the solution. The solution was then heated overnight at ca. 400 K to promote esterification between EG and CA, yielding a glassy resin. The resin was calcined at ca. 623 K in a mantle heater to complete decomposition. Finally, the resulting black powder was calcined on an Al_2O_3 plate at 1123 K for 10 h in air. The as-synthesized powder was confirmed by XRD and EDX to be a solid solution of Rh_2O_3 and Cr_2O_3 ($\text{Rh}_{0.5}\text{Cr}_{1.5}\text{O}_3$).
- (22) Zhang, Y. C.; Kershaw, R.; Dwight, K.; Wold, A. *J. Less-Common Met.* **1988**, 142, 155.
- (23) Brinen, J. S.; Melera, A. *J. Phys. Chem.* **1972**, 76, 2525.
- (24) Abe, Y.; Kato, K.; Kawamura, M.; Sasaki, K. *Surf. Sci. Spectra* **2001**, 8, 117.
- (25) Lide, D. R. *Handbook of Chemistry and Physics*, 83rd ed.; CRC Press: Boca Raton, FL, 2002.